Sustainable Energy & Fuels

ROYAL SOCIETY OF CHEMISTRY

PAPER

View Article Online
View Journal

Cite this: DOI: 10.1039/d6se00450d

Creation of anaerobic microenvironments by photosystem I in porous glass nanopores enables photoinduced H_2 evolution under aerobic conditions

Makoto Hirano, [a] Tomoyasu Noji, [bc] Keisuke Kawakami, [d] Tetsuro Jin, [e] Nobuo Kamiya [f] and Yutaka Amao *[af]

Under aerobic conditions, artificial photosynthesis devices must maintain a steady electron flow toward H_2 evolution. Dissolved O_2 competes for photogenerated electrons, diverting them into oxygen reduction pathways instead of hydrogen production. In this study, we immobilized photosystem I (PSI) in a porous glass plate (PGP) with 50 nm diameter through-thickness nanopores and analyzed electron transfer using transient absorption kinetics. A kinetic model resolves three processes following charge separation: charge recombination with rate constant k_1, electron loss from the terminal iron–sulfur cluster F_B^- in the reduced state to external oxidants, including O_2, with rate constant k_2, and re-reduction of the oxidized reaction center chlorophyll P700 by an external electron donor with rate constant k_3. Remarkably, illumination of a device in which PSI is immobilized in the PGP caused the rate constant k_2 to decrease from 6.5 s^{-1} at 0 min to 1.2–1.3 s^{-1} after 7–10 min. This shows that photochemical O_2 consumption by PSI decreases the intrapore O_2 concentration, suppressing electron transfer from F_B^- to oxidants. Combined with diffusion-limited O_2 delivery, a local low-O_2 microenvironment is formed within the nanopores over time. Extending this concept to a PSI–Pt nanoparticle assembly (PSI–PtNP), we observed sustained light-driven H_2 evolution under aerobic conditions in PGP-immobilized PSI–PtNP, whereas the bulk solution showed much lower activity under aerobic conditions. The system achieved a turnover number of 400 ± 100 mol H_2 per mol PSI and an O_2 tolerance of 44 ± 15%. These findings establish a framework for reaction field engineering in nanopores and guide the design of oxygen-tolerant systems.

Received 20th April 2026
Accepted 1st June 2026

DOI: 10.1039/d6se00450d

rsc.li/sustainable-energy

Introduction

Artificial photosynthesis has attracted remarkable attention as a strategy for producing solar fuels, particularly H_2, from water using sunlight.[1,2] A key challenge for practical deployment lies not only in achieving high activity under inert atmospheres but also in selectively directing photogenerated high-energy electrons toward the desired reaction while suppressing deactivation and competing pathways under aerobic conditions (Fig. 1a).[3–5] In natural photosynthesis, the light reactions proceed through the coordinated action of photosystem II (PSII) and photosystem I (PSI) (Fig. 1b), both embedded in the thylakoid membrane.[6–8] PSII oxidizes water to generate electrons, which are relayed *via* quinones and the cytochrome b_6f complex to plastocyanin (PC) or cytochrome c_6 (cyt c_6), and subsequently to PSI. PSI catalyzes light-driven electron transfer from PC/cyt c_6 on the lumenal side to ferredoxin on the stromal side, thereby supplying reducing equivalents for downstream metabolism. Upon photoexcitation of the reaction center chlorophyll pair P700, an electron is transferred sequentially to A_0, A_1, and the [4Fe–4S] clusters (F_X, F_A, and F_B), generating the charge-separated state $P700^+/F_B^-$ (Fig. 1c).[9–11] Because charge recombination between $P700^+$ and the reduced forms of the intermediate cofactors is approximately 1000 times slower than the forward electron transfer, the photochemical quantum yield for formation of $P700^+/F_B^-$ from the ground state is essentially unity.[12]

Thus, PSI combines efficient light harvesting with highly efficient charge separation and has been widely employed in biohybrid and semi-artificial photochemical systems.[13,14] On

[a]Graduate School of Science, Osaka Metropolitan University, 3-3-138 Sugimoto, Sumiyoshi-ku, Osaka, Japan. E-mail: amao@omu.ac.jp
[b]Department of Applied Chemistry, The University of Tokyo, 7-3-1 Hongo, Bunkyo-ku, Tokyo 113-8654, Japan
[c]Research Center for Advanced Science and Technology, The University of Tokyo, 4-6-1 Komaba, Meguro-ku, Tokyo 153-8904, Japan
[d]Biostructural Mechanism Laboratory, RIKEN SPring-8 Center, 1-1-1 Kouto, Sayo, Hyogo 679-5148, Japan
[e]Nanomaterials Research Institute (NMRI), National Institute of Advanced Industrial Science and Technology (AIST), 1-8-31 Midorigaoka, Ikeda, Osaka 563-8577, Japan
[f]Research Centre for Artificial Photosynthesis, Osaka Metropolitan University, 3-3-138 Sugimoto, Sumiyoshi-ku, Osaka 558-8585, Japan

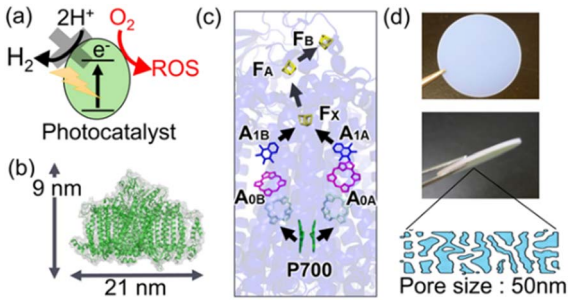

Fig. 1 (a) Illustration of oxygen inhibition in photocatalytic H_2 evolution by O_2. (b) Structure of PSI (PDB ID 1JB0).[10] (c) Electron transfer chains in the reaction center. (d) Photographs of the surface and cross-section of the PGP, and a schematic illustration of the nanopore distribution in the PGP.

this basis, PSI conjugates have been extensively investigated for light-driven H_2 production by coupling PSI with proton reduction catalysts, including hydrogenases,[15,16] metal complexes,[17,18] and Pt-based[19–22] catalysts. In these systems, cyt c_6 (or PC) typically serves as the electron donor. Although high activities have been demonstrated, many studies have been carried out under anaerobic conditions to avoid oxygen inhibition. Two strategies have been proposed to mitigate oxygen inhibition. One approach is to endow the hydrogen evolution catalyst itself with oxygen tolerance. Recently, Rumbaugh *et al.* reported that a PSI–hydrogenase complex, in which the O_2-tolerant [FeFe] hydrogenase was fused to the stromal-side PSI subunit PsaE, retained 2.3% of its H_2 evolution activity under aerobic conditions relative to that under anaerobic conditions (*i.e.*, oxygen tolerance).[23] Another approach is to engineer the reaction environment to create a localized low-oxygen microenvironment. In recent microreactor and cell coating systems using living algal cells, low-oxygen regions can form near cells or within aggregates even under air, enabling light-driven H_2 production by activating hydrogenase and suppressing its inactivation, thereby sustaining and enhancing H_2 generation.[24,25]

Creating localized low-oxygen microenvironments under artificial (cell-free) conditions is advantageous because it can be combined with catalyst-level oxygen tolerance. We have previously shown that immobilizing photosensitizers/hydrogenase (or formate dehydrogenase) or PSI–Pt nanoparticle conjugates (PSI–PtNP) within the porous glass plates (PGPs) enables light-driven H_2 or formate production under aerobic conditions.[26–28] PGPs[26–29] are optically transparent in the visible region and contain through-thickness nanopores with high internal surface area, allowing immobilization of photochemical components within a light-transmitting solid support (Fig. 1d). To advance strategies that mitigate oxygen inhibition by forming localized anaerobic microenvironments, quantitative analysis of PGP-based photoreaction systems is essential. Here, we combine time-resolved spectroscopy with biohybrid device construction in a nanoporous platform to elucidate the mechanism of microenvironment formation. PSI is immobilized within the nanopores of PGPs, and light-induced electron transfer branching is quantified by transient absorption spectroscopy (TAS) and analyzed using a kinetic framework that resolves charge recombination,[22] electron transfer to external acceptors including O_2,[30] and reduction of oxidized P700 by external donors.[31] By comparing aerobic and anaerobic conditions and tracking illumination-dependent changes under aerobic conditions, we clarify how confinement alters the external acceptor pathway in a nanoporous environment. We then extend this approach to a PSI–PtNP system immobilized in a PGP to evaluate light-driven H_2 evolution, directly comparing immobilized and solution-phase systems while optimizing immobilization for uniform distribution of PSI–PtNP and cyt c_6 within the porous matrix.

Experimental section

Purification of PSI

PSI was isolated from the cyanobacterial membranes of *T. vulcanus*.[32] Purified PSI was solubilized in 40 mmol per L 4-(2-hydroxyethyl)-1-piperazineethanesulfonic acid (HEPES)–NaOH (pH 7.8) containing 50 mmol per L NaCl and 0.03% (w/v) *n*-dodecyl-β-D-maltoside (DM). The PSI concentration was determined *via* UV-vis absorption spectroscopy using an extinction coefficient (ε) of 16.4 L μmol^{-1} cm^{-1} (PSI monomer equivalent)[33] with a double-beam spectrophotometer (UV-1800 PC, SHIMADZU, Japan).

Preparation of a PGP

A PGP, 1 mm × 4 cm × 4 cm, with an average pore diameter of 50 nm was prepared by acid leaching of phase-separated borosilicate glass, as previously described.[34,35] The parent glass (62.5 SiO_2, 28.3 B_2O_3, and 9.2 Na_2O; wt%) was melted in a platinum crucible and heat-treated at 610 °C for 32 h to induce phase separation. The resulting glass was then leached in 1 N H_2SO_4 at 90 °C for 2 days. The pore diameter, pore volume, and specific surface area of the PGP were determined *via* mercury intrusion porosimetry, as described previously.[26]

Preparation and characterization of PtNPs

PtNPs were prepared according to previously reported methods.[36] The particle size of the PtNPs was determined by dynamic light scattering (DLS) using an ELSZ-2000 ZS instrument (Otsuka Electronics, Japan) and by transmission electron microscopy (TEM) using a JEM-1010 microscope (JEOL, Japan).

Preparation of cyt c_6

cyt c_6 from *Synechocystis* sp. PCC 6803 was cloned and heterologously expressed in *E. coli* according to previous reports and purified by Ni^{2+} affinity chromatography.[37–39]

Preparation of PSI–PtNP

PSI–PtNP was prepared according to previous reports.[20] PSI (1 $\mu mol\ L^{-1}$) and PtNPs (2 $\mu mol\ L^{-1}$) were mixed in buffer (40 mmol per L HEPES–NaOH, pH 7.8, 50 mmol per L NaCl, 0.03% [w/v] DM) and stirred at 4 °C for 2 h in the dark. Unbound

PtNPs were removed using an Amicon Ultra-50 kDa filter (Merck).

Negative-stain TEM imaging and two-dimensional (2D) classification of PSI and PSI–PtNP

Negative-stain TEM was used to examine the morphology of PSI and PSI–PtNP. Samples were applied to TEM grids, negatively stained with 2% (w/v) aqueous ammonium molybdate for 30 s, and then imaged. For PSI, single-particle analysis was performed using Scipion,[40] with particle picking and extraction carried out in Xmipp.[41] The extracted particles were subjected to 2D classification in RELION[42] using only particle images with *Z*-scores of <3.

Transient absorption spectroscopy

TAS measurements of PSI were conducted in a measurement buffer (40 mmol per L HEPES–NaOH, pH 7.8, containing 0.03% (w/v) DM, 10 mmol per L ascorbic acid and 0.1 mmol per L 2,6-dichloroindophenol [DCIP]) using a 1 cm pathlength quartz cuvette. For PGP measurements, the plate was incubated at 4 °C for 1 h in the same buffer containing 5.8 μmol per L PSI. It was rinsed and placed in a 2 mm pathlength quartz cell filled with the measurement buffer. Anaerobic samples were prepared by keeping the samples overnight in the dark in an N_2-filled glovebox. TAS was performed with a 700 nm probe from a halogen lamp and excitation using a xenon flash lamp (1 μs pulse) filtered to 400–500 nm at 0.2 Hz. The transmitted probe intensity was detected with a photomultiplier tube through a 700 nm filter. Signals were recorded with a digital oscilloscope at 10 μs time resolution up to 4 s, averaged over 128 shots, and fitted to multiexponential functions (OriginLab).

Electron transfer kinetics

The redox state of the P700/F_B pair is represented as [P700–F_B]. After charge separation, PSI is generated in the state [$P700^+$–F_B^-].

Here, [$P700^+$–F_B^-] and [$P700^+$–F_B] are time-dependent concentrations. This state relaxes through two competing pathways. First, the electron on F_B^- can return to $P700^+$, leading to charge recombination; the corresponding rate constant is defined as k_1 (s^{-1}). Second, the electron on F_B^- can be transferred to an external electron acceptor; the rate constant for this process is defined as k_2 (s^{-1}). Reported external acceptors for PSI include dissolved oxygen and oxidized ascorbic acid.[30,43] Electron transfer to the external acceptor converts [$P700^+$–F_B^-] to [$P700^+$–F_B]. Finally, $P700^+$ is re-reduced by ascorbate through DCIP-mediated electron transfer,[31] with a rate constant k_3 (s^{-1}), returning the system to [P700–F_B].

In principle, [P700–F_B^-] can be formed when $P700^+$ is reduced by the donor-side pathway before F_B^- is oxidized. Under the present conditions, this process is assigned to the slow kinetic component with a rate constant of approximately 0.5 s^{-1} (Table S1). In contrast, electron transfer from F_B^- to external electron acceptors proceeds with a rate constant of approximately 6–7 s^{-1}. Thus, donor-side reduction of $P700^+$ is more than one order of magnitude slower than electron transfer from F_B^- to external acceptors. Therefore, the simplified kinetic model focuses on the main decay pathways of [$P700^+$–F_B^-], namely charge recombination and electron transfer to external acceptors.

Based on this scheme, we formulated rate equations for the relevant PSI redox states, including the $P700^+$-containing species [$P700^+$–F_B^-] and [$P700^+$–F_B], as well as [P700–F_B^-]:

$$\frac{d[P700^+ - F_B^-]}{dt} = -(k_1 + k_2 + k_3)[P700^+ - F_B^-] \quad (1)$$

$$\frac{d[P700^+ - F_B]}{dt} = -k_3[P700^+ - F_B] + k_2[P700^+ - F_B^-] \quad (2)$$

$$\frac{d[P700 - F_B^-]}{dt} = -k_2[P700 - F_B^-] + k_3[P700^+ - F_B^-] \quad (3)$$

The total concentration of PSI in the $P700^+$ state is given by:

$$[P700^+] = [P700^+–F_B^-] + [P700^+–F_B] \quad (4)$$

Substituting the analytical solutions of [$P700^+$–F_B^-] and [$P700^+$–F_B] (derived in the SI, eqn (S1)–(S8)) into eqn (4) yields:

$$[P700^+] = [P700^+ - F_B^-]_0\left(\frac{k_1}{k_1 + k_2}e^{-(k_1+k_2+k_3)t} + \frac{k_2}{k_1 + k_2}e^{-k_3 t}\right) \quad (5)$$

where [$P700^+$–F_B^-]$_0$ indicates the initial concentration after charge separation, and [$P700^+$–F_B^-], [$P700^+$–F_B], and [$P700^+$] are time-dependent concentrations. Eqn (5) shows that the decay of the PSI population with $P700^+$ after charge separation is described by a bi-exponential function. To experimentally monitor this time dependence, we performed TAS by detecting the absorbance change and converting it to [$P700^+$] using the Beer–Lambert law. Absorbance changes at 700 nm provide a clear P700/$P700^+$ difference signal and enable monitoring of the $P700^+$ population in PSI. $P700^+$–P700 difference spectra of PSI have been reported previously, and changes around 700 nm are widely used to follow the P700/$P700^+$ redox transition.[44]

Light-driven hydrogen evolution

The light source for the light-driven H_2 evolution experiments was a solar simulator (HAL-320, Asahi Spectra). After calibration, an RG610 filter (HOYA), a heat-cut filter (HA50, HOYA), and a neutral-density filter (ND30, HOYA) were installed in the light path. The emission spectrum of the light source was measured using a fiber-optic spectrometer (SILVER-NOVA, StellarNet). Under these conditions, the photon flux density in the 400 to 700 nm range was 230 μmol m^{-2} s^{-1} and the irradiance was 44 W m^{-2}. For the solution system, 3 mL of a PSI–PtNP suspension (30 nmol per L PSI–PtNP, 100 mmol per L ascorbic acid, 0.03% (w/v) DM, 4 μmol per L cyt c_6, 20 mmol per L 2-(*N*-morpholino)ethanesulfonic acid (MES)–NaOH, pH 6.2) was placed in a 5 mL vial, sealed with a butyl septum, and stirred. Anaerobic samples were prepared by bubbling N_2 for 45 min. For immobilized experiments, a PGP was incubated in a PSI–PtNP solution (2.9 μmol per L PSI–PtNP in 20 mmol per L

MES–NaOH, pH 6.2, containing 0.03% (w/v) DM) at 4 °C for 1 h in the dark, rinsed, and then incubated overnight in a cyt c_6 solution (100 μmol per L cyt c_6, 100 mmol per L ascorbic acid, 20 mmol per L MES–NaOH, pH 6.2, 50 mmol per L NaCl). After rinsing, the plate was immersed in 3 mL of reaction solution (100 mmol per L ascorbic acid, 4 μmol per L cyt c_6, 20 mmol per L MES–NaOH, pH 6.2) in an 8 mL vial and sealed. Anaerobic samples were prepared by bubbling N_2 for 45 min. H_2 was quantified by withdrawing 100 μL of headspace gas with a gastight syringe and analyzing it by GC (GC-2010, Shimadzu). Turnover number (TON) was calculated from the amount of H_2 produced after 10 h of illumination. TON and O_2 tolerance were calculated using eqn (S9) and (S10).

Results and discussion

TAS measurements of PGP-immobilized PSI

From the UV-vis absorption spectrum of PGP-immobilized PSI (Fig. 2a), the amount of immobilized PSI was estimated, giving an intrapore PSI concentration of 0.57 μmol L^{-1}, which corresponds to 0.20 μmol PSI per m^2 (Fig. S1). In this study, PSI was used for TAS measurements to simplify the interpretation of $P700^+$ decay. In PSI–PtNP, electron transfer from F_B^- to PtNPs and possible back electron transfer from PtNPs to PSI can occur in addition to electron transfer from F_B^- to dissolved O_2. These processes overlap in the 700 nm $P700^+$ transient absorption signal and cannot be separated by the present analysis. Therefore, PSI was used as a simplified model to evaluate the effect of the PGP nanopore environment on the external electron-acceptor pathway.

Next, for analyzing the electron transfer pathways from the terminal acceptor F_B following charge separation between the primary donor P700 and F_B in the PSI reaction center, we adopted the kinetic scheme shown in Fig. 2b. Based on eqn (5), the transient absorption decay time courses monitored at 700 nm were fitted to obtain the rate constants k_1, k_2, and k_3, enabling a comparison between PSI in solution and PSI immobilized in a PGP. Furthermore, to evaluate the effect of light irradiation on the kinetics of PSI in solution and PGP-immobilized PSI, respectively, under aerobic conditions, samples were pre-irradiated for 0–10 min prior to TAS measurements (Fig. S2 and S3). The resulting rate constants are summarized in Table 1.

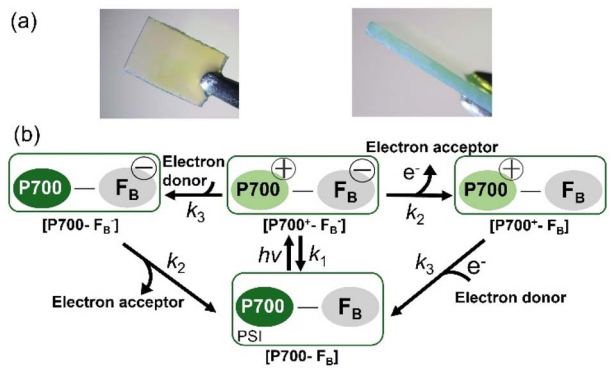

Fig. 2 (a) Photographs of the PGP sample after PSI immobilization, showing the surface and side views. (b) Kinetic scheme describing light-induced charge separation and subsequent branching processes in PSI: charge recombination of the [$P700^+$–F_B^-] state (rate constant k_1), electron transfer from F_B^- to external electron acceptors (k_2), and reduction of oxidized $P700^+$ by an external electron donor (k_3).

For PSI in solution under aerobic conditions (Fig. 3a), k_1 = 6.6 s^{-1} and k_2 = 6.2 s^{-1} were obtained (Table 1), and k_3 = 0.49 s^{-1} (Table S1). Previous work has shown that the charge-separated state $P700^+$–F_B^- undergoes charge recombination with a time constant of 65 ms.[22] This corresponds to the rate constant of approximately 15 s^{-1}, and the k_1 values obtained in this study are of the same order of magnitude. For PSI in solution, the TAS kinetic traces were unchanged across the tested pre-irradiation times for 0–10 min (Fig. 3a). The fitted rate constants remained constant, with k_1 = 6.4–6.8 s^{-1}, k_2 = 6.2–6.3 s^{-1}, and k_3 = 0.49–0.51 s^{-1} over 0–10 min (Fig. 3c, d, Tables 1, and S1). Thus, under these conditions, pre-irradiation does not affect electron transfer kinetics of PSI in solution. This negligible time dependence in solution can be explained quantitatively by the larger O_2/PSI molar ratio and mechanistically by rapid O_2 resupply under homogeneous conditions. For the solution system, the PSI concentration was 180 nmol L^{-1}. Using an air-saturated O_2 concentration of 253 μmol L^{-1} at 25 °C, the initial O_2/PSI molar ratio in solution was approximately 1.4 × 10^3. In addition, O_2 consumed by PSI in solution can be rapidly replenished from the surrounding solution and gas phase. Consistently, in a separate O_2 sensor measurement under aerobic illumination, the dissolved O_2 concentration in PSI solution decreased by only 15–18 μmol L^{-1} and then reached a plateau (Fig. S4). This decrease corresponds to only 6–7% of the initial dissolved O_2 concentration, indicating that sufficient O_2 remained in solution and that the local O_2 concentration around PSI did not decrease enough to change k_2 detectably. In contrast, PGP-immobilized PSI exhibited a pronounced illumination history dependence (Fig. 3b), with a progressive decrease in k_2 (Fig. 3c). Specifically, k_2 decreased from 6.5 s^{-1} at 0 min to 4.8 s^{-1} at 1 min, 2.4 s^{-1} at 2 min, and 1.7 s^{-1} at 3 min, followed by a slower decline to 1.3 s^{-1} at 5 min and a near plateau of 1.2–1.3 s^{-1} at 7–10 min (Fig. 3c and Table 1). By comparison, k_1 remained within 3.0–3.8 s^{-1} over the same

Table 1 Rate constants k_1 and k_2 obtained by fitting the transient absorption time courses of PSI in solution and PGP-immobilized PSI. Rate constant k_3 is shown in Table S1

		Rate constant (s^{-1})			
		k_1		k_2	
Condition	Pre-irradiation time (min)	Solution	PGP	Solution	PGP
Aerobic	0	6.6	3.6	6.2	6.5
	1	6.8	3.0	6.3	4.8
	2	—	3.6	—	2.4
	3	6.5	3.6	6.2	1.7
	5	6.7	3.6	6.3	1.3
	7	—	3.6	—	1.3
	10	6.7	3.8	6.2	1.2
Anaerobic		6.4	3.8	1.0	2.3

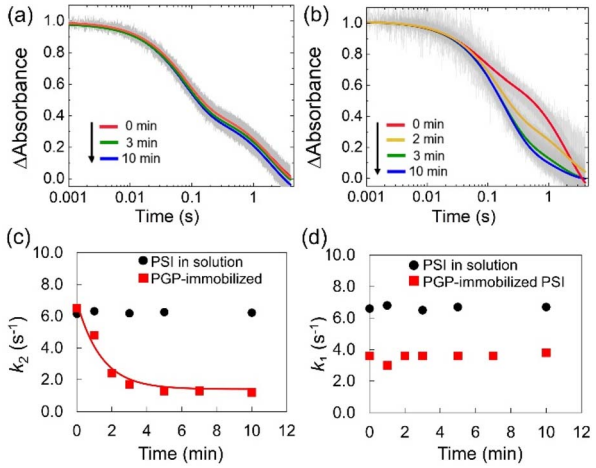

Fig. 3 Pre-irradiation time dependence of transient absorption decay in PSI. (a) Transient absorption decay time courses of PSI in solution recorded after 0, 3, and 10 min of pre-irradiation. (b) Corresponding time courses for PGP-immobilized PSI recorded after 0, 2, 3, and 10 min of light pre-irradiation. Gray lines show experimental results. Colored lines represent the best–fit curves obtained using eqn (5). Fitting parameters are shown in Tables 1 and S1. (c) Time dependence of k_2. The red line represents the best–fit curve obtained using eqn (7) and (8). Fitting parameters are shown in Table 2. (d) Time dependence of k_1.

interval (Fig. 3d and Table 1), indicating that light pre-irradiation mainly perturbs the pathway represented by k_2 in the PGP system. Consistent with this trend, the branching fraction, $k_2/(k_1 + k_2) \times 100$, decreased from 64% at 0 min to ~25% at 5–10 min for PGP-immobilized PSI, whereas it remained essentially constant at 48–49% for PSI in solution. These results indicate that the contribution of external acceptor pathways diminishes with illumination time only in the immobilized system. Because k_2 reflects electron transfer to external acceptors, the progressive decrease in k_2 for PGP-immobilized PSI suggests that the external acceptor branch becomes less accessible.

Next, transient absorption kinetics were measured under anaerobic conditions. Under anaerobic conditions, both PSI in solution and PGP-immobilized PSI exhibited decay profiles similar to those observed for PGP-immobilized PSI after pre-irradiation under aerobic conditions (Fig. 4). Fitting the time courses measured under anaerobic conditions yielded smaller k_2 values than those under aerobic conditions (Table 1), indicating that dissolved O_2 is the primary external electron acceptor under aerobic conditions. Even under anaerobic conditions, k_2 was not 0, suggesting that other electron acceptors, such as oxidized ascorbic acid, may contribute.[43] Because the light intensity used for pre-irradiation was sufficiently high and not rate-limiting for the photoreaction, we assumed that PSI effectively operated in an excited-state regime. Under this approximation, the intrapore dissolved oxygen concentration, $[O_2]_{pore}$, is expected to follow first-order decay (eqn (6) and (7)):

$$\frac{d[O_2]_{pore}}{dt} = k_i\left([O_2]_{bulk} - [O_2]_{pore}\right) - k_{O_2}[PSI][O_2]_{pore} \quad (6)$$

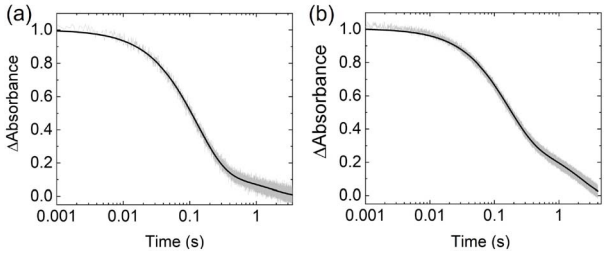

Fig. 4 Transient absorption time courses of PSI under anaerobic conditions. (a) PSI in solution. (b) PGP-immobilized PSI. Gray lines show experimental results. Black lines represent the best–fit curves using eqn (5). Fitting parameters are shown in Tables 1 and S1.

where [PSI] is the PSI concentration (0.57 μmol L^{-1} in this study) and $[O_2]_{bulk}$ is the dissolved oxygen concentration in bulk solution (253 μmol L^{-1} at 25 °C),[45] k_i is an apparent first-order rate constant for oxygen transport from a bulk solution into PGP nanopores, and k_{O_2} is an effective second-order rate constant for PSI-driven O_2 reduction (L μmol^{-1} s^{-1}). Assuming that the oxygen concentration in the PGP nanopores before pre-irradiation is the same as that in the bulk solution, eqn (6) gives the following expression for the nanopore oxygen concentration as a function of illumination time.

$$[O_2]_{pore}(t) = [O_2]_{bulk}\left[\frac{k_i}{k_i + k_{O_2}[PSI]} + \frac{k_{O_2}[PSI]}{k_i + k_{O_2}[PSI]}\exp(-(k_i + k_{O_2}[PSI])t)\right] \quad (7)$$

The rate constant k_2 for electron loss from PSI to external electron acceptors can be decomposed into electron loss to O_2 and nonoxygen external acceptors, X:

$$k_2 = k_{O_2}[O_2] + k_x[X] \quad (8)$$

Here, [X] and k_x denote the concentration of the external electron acceptor and the rate constant for electron transfer to X, respectively; because X is present in large excess in our experiments, both can be treated as time-independent constants. By substituting $[O_2]_{pore}$ from eqn (7) into $[O_2]$ in eqn (8) and fitting the illumination time dependence of k_2 measured for PGP-immobilized PSI (Fig. 3c) with the constraint $k_i \geq 0$, we obtained $k_x[X] = 1.4\ s^{-1}$, which falls within the range of $k_2 = 1$–$2.3\ s^{-1}$ under anaerobic conditions (Table 1). In this fit, $k_{O2}[PSI] = 0.012\ s^{-1}$ and $k_i = 0\ s^{-1}$ (Table 2). Because k_i cannot be assumed to be 0, this result suggests that $k_{O2}[PSI]$ is significantly faster than k_i.

Table 2 Fitting parameters of the k_2 time course of PGP-immobilized PSI

Parameter	Value [unit]
k_{O2}	0.021 [L (μmol)$^{-1}$ s^{-1}]
k_i	0 [s^{-1}]
$k_x[X]$	1.4 [s^{-1}]

Therefore, the observation that k_2 slowed upon pre-illumination only in PGP-immobilized PSI indicates that the rate of PSI-driven photoreduction of oxygen is faster than the rate of oxygen supply into the PGP nanopores. The estimated intrapore PSI concentration in PGP was 0.57 μmol L^{-1}, giving an initial O_2/PSI molar ratio of approximately 4.4×10^2. Thus, even before illumination, the O_2/PSI molar ratio in the PGP nanopores was approximately threefold lower than that in homogeneous solution. Furthermore, in the homogeneous solution system, O_2 supply from the gas phase to the liquid phase can largely compensate for PSI-driven O_2 consumption, resulting in only a small apparent change in the dissolved O_2 concentration. By contrast, O_2 supply from the bulk liquid phase into the liquid confined within the nanopores is sufficiently restricted relative to the O_2 consumption process. Therefore, immobilization of the photochemical reaction system in PGP can substantially suppress O_2 supply from the O_2-rich external environment to the local environment surrounding the O_2-sensitive photochemical components.

Photoreduction of O_2 by PSI may generate reactive oxygen species, such as superoxide and H_2O_2.[3] These ROS may contribute to deactivation of PSI, cyt c_6, or PtNPs during prolonged irradiation. However, ROS were not directly quantified in this study, and their concentration and specific effects inside the PGP nanopores remain unclear. Direct quantification of ROS within the nanopore environment will be an important subject for future work. Previous studies have reported that the lifetime of reduced methyl viologen, a highly oxygen-sensitive species, is markedly prolonged upon immobilization within PGP nanopores and reaches on the order of hours compared with that in solution, which suggests that oxygen transport from the bulk solution into the nanopores is diffusion-limited.[26] Thus, intrapore oxygen consumption during illumination may outpace oxygen supply from the bulk solution, creating a transport bottleneck and causing k_2 to decrease. Conversely, in bulk solution, any local O_2 consumption would be rapidly compensated by diffusion and gas–liquid equilibration, consistent with the negligible time dependence of k_2.

Light-driven H_2 evolution

PtNPs with an average diameter of approximately 2 nm were characterized using TEM and DLS, and negative-stain TEM supported their binding to PSI trimers (Fig. S5–S10). UV-vis spectral overlay analysis after removal of unbound PtNPs supported a PtNP/PSI ratio of 1 : 1 on a PSI monomer-equivalent basis, corresponding to approximately three PtNPs per PSI trimer (Fig. S11). The PSI–PtNP interaction is considered to be mainly electrostatic because the PtNP surface is expected to be negatively charged owing to thiomalate-derived carboxylate groups. This interpretation is consistent with previous PSI–PtNP studies showing that carboxylate-covered PtNPs bind to the stromal-side electron-acceptor region of PSI.[20,21] Therefore, the TEM images are used as qualitative evidence supporting PSI–PtNP binding, whereas the PtNP/PSI ratio was estimated from UV-vis spectral overlay analysis. Absorption spectral analysis showed that the immobilization amounts of PSI–PtNP and cyt c_6 in PGP were 17 ± 0.5 μmol PSI–PtNP per m^2 and 0.31 ± 0.04 mmol cyt c_6 per m^2, respectively (Fig. S12), which correspond to an intrapore PSI–PtNP concentration of 0.24 ± 0.01 μmol L^{-1}. The aerobic H_2-evolution experiments were performed in sealed vials with an air headspace. The O_2 amount in the headspace was approximately 1.9×10^5 equivalents relative to PSI–PtNP, indicating that O_2 was present in large excess under the sealed aerobic conditions. Under aerobic conditions, photoinduced H_2 evolution from PGP-immobilized PSI–PtNP continued for 30 h, whereas in the solution system, the amount of evolved H_2 was below the detection limit (Table 3 and Fig. S13). Even when stirring was applied to increase the reaction rate in the solution system, photoinduced H_2 evolution ceased after 10 h (Fig. S13). Under aerobic conditions, TON during 10 h of light irradiation was 400 ± 100 mol H_2 per mol PSI for PGP-immobilized PSI–PtNP and 170 ± 20 mol H_2 per mol PSI for the stirred solution system (Table 3 and Fig. S13). These values, relative to the TON under anaerobic conditions, were 44 ± 15% for PGP-immobilized PSI–PtNP and 5.0 ± 0.8% for the stirred solution system (Table 3 and Fig. S13). This result indicates that the reaction system in the PGP nanopores exhibited ninefold higher oxygen tolerance than the solution system (Table 3). Under anaerobic conditions, the TON = 900 ± 200 mol H_2 per mol PSI for PGP-immobilized PSI–PtNP was comparable to 800 ± 200 mol H_2 per mol PSI of the unstirred solution system, suggesting that immobilization in the porous glass plate does not impose a substantial additional kinetic limitation under quiescent conditions. In contrast, stirring markedly increased the activity in bulk solution, indicating that H_2 evolution under unstirred conditions is limited by mass transport and/or diffusional encounters among PSI–PtNP, cyt c_6, and redox components (Table 3 and Fig. S13).

Compared with the previously reported PGP50 system[28] in which PSI–PtNP and cyt c_6 were co-immobilized, the PGP system developed here showed 2.4-fold higher activity under anaerobic conditions and 6.7-fold higher activity under aerobic conditions. O_2 tolerance also increased from 16% to 44 ± 15%, corresponding to a 2.8-fold improvement. In conventional co-immobilization based on simultaneous adsorption, cyt c_6 tends to localize deeper in the nanopores, whereas PSI–PtNP accumulates near the PGP surface;[28] conversely, sequential immobilization of PSI–PtNP followed by cyt c_6 resulted in a more homogeneous intrapore distribution (Fig. S14), which suggests more frequent PSI–cyt c_6 encounters.

Table 3 TON during 10 h of light irradiation and O_2 tolerance for light-driven H_2 evolution by PSI–PtNP in solution and in the PGP under anaerobic and aerobic conditions

		TON (mol H_2 per mol PSI)		
System	Condition	Anaerobic	Aerobic	O_2 tolerance (%)
PGP	Without stirring	900 ± 200	400 ± 100	44 ± 15
Solution	Without stirring	800 ± 200	N.D.[a]	N.A.[b]
	With stirring	3400 ± 400	170 ± 20	5.0 ± 0.8

[a] N.D., not detected. [b] N.A., not applicable.

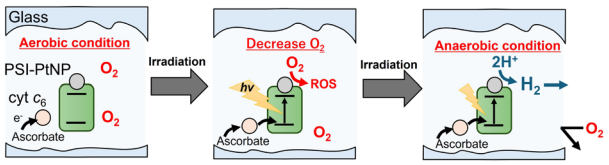

Fig. 5 Proposed mechanism for oxygen-tolerant light-driven H_2 evolution in PGP-immobilized PSI–PtNP.

In this study, we integrated the TAS of PSI immobilized in PGPs under aerobic conditions with the light-driven H_2 evolution results to discuss the mechanism by which the PSI–PtNP/PGP system retains activity under aerobic conditions (Fig. 5). Initially, O_2 is present within the nanopores. During photoirradiation, photogenerated reducing equivalents are consumed by O_2 reduction in the pore space, whereas O_2 influx from the bulk is diffusion-limited within the porous matrix. Consequently, the intrapore O_2 concentration is expected to decrease during irradiation, establishing an effectively anaerobic microenvironment within the pores. Under such intrapore conditions, competitive electron loss to O_2 is mitigated, allowing productive electron transfer to proceed from cyt c_6 to PSI–PtNP, thereby enabling H_2 evolution even under aerobic conditions.

Previous studies in which photochemical reaction systems were introduced into PGPs have shown that reducing the pore diameter to approximately 20 nm limits the immobilization of photosynthetic membrane protein complexes, whereas reducing the plate thickness to approximately 0.2 mm decreases the amount of immobilized molecules.[26,29] Therefore, based on these previous studies, we used a PGP with a thickness of 1 mm and a pore diameter of 50 nm in this study. These dimensions were appropriate because the 50 nm pores were sufficiently large to accommodate PSI–PtNP and cyt c_6 without severely limiting immobilization, while being sufficiently small to restrict O_2 supply from the bulk solution. Thus, this PGP design enabled the formation of a local low-O_2 environment around the photochemical reaction system, leading to the observed oxygen-shielding effect.

However, we do not claim that this effect is unique to the PGP. Rather, the PGP served as a useful model platform for elucidating the mechanism by which light-driven H_2 evolution can be enabled under aerobic conditions by lowering the local O_2 concentration around the photochemical reaction system. In fact, recent microreactor and cell-coating systems using living algal cells have shown that low-O_2 regions can form near cells or within aggregates, thereby enabling light-driven H_2 production.[24,25] A key requirement common to our study and these previous studies is that the platform and the photochemical reaction system should be designed so that local O_2 consumption exceeds O_2 resupply from the O_2-rich external environment. In this respect, the PGP is a suitable porous material because it simultaneously satisfies the requirements of visible-light transparency, an appropriate pore diameter that is neither too large nor too small, a large internal surface area, protein compatibility, and an appropriate plate thickness.

Conclusions

In this study, PSI was immobilized within the 50 nm nanopores of a porous glass plate and analyzed *via* TAS. Light-driven H_2 evolution by PSI–PtNP was also compared under aerobic and anaerobic conditions. The transient absorption kinetics were analyzed using a scheme comprising charge recombination of the charge-separated state $P700^+$–F_B^- with rate constant k_1, electron transfer from F_B^- to external electron acceptors with k_2, and reduction of $P700^+$ by an external electron donor with k_3. Under aerobic conditions with pre-irradiation, the PSI solution system kinetics demonstrated negligible time dependence because the rate of O_2 supply from the gas phase to the liquid phase competes with the rate of PSI-driven O_2 consumption. Whereas the immobilized system showed a clear minute-scale decrease in k_2 from 6.5 s^{-1} at 0 min to 1.2–1.3 s^{-1} after 7–10 min, indicating a reduction in electron loss rate to external electron acceptors (primarily O_2), as reflected by a decrease in $k_2/(k_1 + k_2) \times 100$ from 64% to ~25%. These results suggest that the rate of O_2 consumption greatly exceeded the rate of O_2 supply from the bulk aqueous phase to the liquid phase inside the nanopores, resulting in a gradual decrease in the intrapore O_2 concentration and, consequently, the formation of a local anaerobic microenvironment within the nanopores. For light-driven H_2 evolution, the solution system exhibited a loss of activity under aerobic conditions, whereas the PSI–PtNP immobilized PGP system maintained H_2 evolution even under aerobic conditions, achieving TON = 400 ± 100 mol H_2 per mol PSI. The O_2 tolerance was 44 ± 15%, corresponding to a nine-fold improvement over the stirred solution system.

Hence, these results provide quantitative kinetic evidence that PSI immobilized in a PGP progressively decreases the intrapore O_2 concentration during illumination, thereby creating locally anaerobic microenvironments within PGP nanopores. We further reveal that immobilization of PSI–PtNP enables light-driven H_2 evolution activity under aerobic conditions. Overall, these findings provide practical design guidelines for controlling intrapore oxygen and electron transfer pathways, facilitating PSI-driven hydrogen evolution under aerobic conditions.

Author contributions

All authors contributed equally to this work. M. H. and T. N. conducted most of the experiments and analyzed the electron transfer kinetics. M. H. drafted the manuscript. T. N. conceived the idea for this work and modified the manuscript. Y. A. supervised the project. N. K. and K. K. provided suggestions for the project. T. J. prepared the PGP. K. K. assisted with PSI preparation. Y. A. finalized the manuscript. All authors discussed the results and provided comments on the manuscript.

Conflicts of interest

There are no conflicts to declare.

Data availability

The authors confirm that the data supporting the findings of this manuscript are available within the article and its supplementary information (SI). Supplementary information: UV-vis spectra, transient absorption time courses, time course of dissolved O_2 concentration, TEM and DLS data, 2D classification results, kinetic derivations (eqn (S1)–(S8)), definitions of TON and O_2 tolerance (eqn (S9) and (S10)), immobilization analysis, hydrogen-evolution data, and additional figures (PDF). See DOI: https://doi.org/10.1039/d6se00450d.

Acknowledgements

This work was supported by JSPS KAKENHI (N. K.) Grant No. 17H03645 and Grant No. 17H06434 in Scientific Research on Innovative Areas "Innovations for Light-Energy Conversion (I^4LEC)." T. N. thanks the Takahashi Industrial and Economic Research Foundation, the Koyanagi Foundation, the Iwatani Naoji Foundation, the Japan Prize Foundation, and the Strategic Research Grant-in-Aid for Young Scientists at Osaka City University for funding. We thank Associate Professor Yoshihiro Yamaguchi (Graduate School of Science, Osaka Metropolitan University, Japan) for access to an electroporation device. We thank Professor Yasuyuki Tsuboi (Graduate School of Science, Osaka Metropolitan University, Japan) for access to DLS facilities. We thank Professor Makoto Miyata and Postdoctoral Researcher Yu-hei Tahara (Graduate School of Science, Osaka Metropolitan University, Japan) for assistance with TEM observations of platinum nanoparticles and PSI–Pt nanoparticle complexes. We thank Professor Hirozo Oh-oka (Graduate School of Science, Osaka University, Japan) for assistance with transient absorption measurements under anaerobic conditions and for providing cyt c_6 samples. We thank Assistant Professor Masaharu Kondo and Professor Takehisa Dewa (Nagoya Institute of Technology, Japan) for helpful discussions and for providing cyt c_6 samples.

References

1 A. Fujishima and K. Honda, *Nature*, 1972, **238**, 37–38.
2 Q. Wang, T. Hisatomi, Q. Jia, H. Tokudome, M. Zhong, C. Wang, Z. Pan, T. Takata, M. Nakabayashi, N. Shibata, Y. Li, I. D. Sharp, A. Kudo, T. Yamada and K. Domen, *Nat. Mater.*, 2016, **15**, 611–615.
3 D. W. Wakerley and E. Reisner, *Energy Environ. Sci.*, 2015, **8**, 2283–2295.
4 M. G. Allan, M. J. McKee, F. Marken and M. F. Kuehnel, *Energy Environ. Sci.*, 2021, **14**, 5523–5529.
5 B. Mondal and A. Dey, *Chem. Commun.*, 2017, **53**, 7707–7715.
6 N. Nelson and A. Ben-Shem, *Nat. Rev. Mol. Cell Biol.*, 2004, **5**, 971–982.
7 N. Nelson and C. F. Yocum, *Annu. Rev. Plant Biol.*, 2006, **57**, 521–565.
8 F. R. Whatley, K. Tagawa and D. I. Arnon, *Proc. Natl. Acad. Sci. U. S. A.*, 1963, **49**, 266–270.
9 U. Schreiber, *Photosynth. Res.*, 2017, **134**, 343–360.
10 P. Jordan, P. Fromme, H. T. Witt, O. Klukas, W. Saenger and N. Krauß, *Nature*, 2001, **411**, 909–917.
11 K. Brettel, *Biochim. Biophys. Acta, Bioenerg.*, 1997, **1318**, 322–373.
12 S. Itoh, M. Iwaki and I. Ikegami, *Biochim. Biophys. Acta, Bioenerg.*, 2001, **1507**, 115–138.
13 L. M. Utschig and K. L. Mulfort, *Chem. Commun.*, 2024, **60**, 10642–10654.
14 P. N. Ciesielski, F. M. Hijazi, A. M. Scott, C. J. Faulkner, L. Beard, K. Emmett, S. J. Rosenthal, D. Cliffel and G. K. Jennings, *Bioresour. Technol.*, 2010, **101**, 3047–3053.
15 C. E. Lubner, P. Knörzer, P. J. N. Silva, K. A. Vincent, T. Happe, D. A. Bryant and J. H. Golbeck, *Biochemistry*, 2010, **49**, 10264–10266.
16 M. Ihara, H. Nishihara, K.-S. Yoon, O. Lenz, B. Friedrich, H. Nakamoto, K. Kojima, D. Honma, T. Kamachi and I. Okura, *Photochem. Photobiol.*, 2006, **82**, 676–682.
17 L. M. Utschig, N. M. Dimitrijevic, O. G. Poluektov, S. D. Chemerisov, K. L. Mulfort and D. M. Tiede, *J. Am. Chem. Soc.*, 2011, **133**, 16334–16337.
18 S. C. Silver, J. Niklas, P. Du, O. G. Poluektov, D. M. Tiede and L. M. Utschig, *J. Am. Chem. Soc.*, 2013, **135**, 13246–13249.
19 N. S. Ponomarenko, N. J. Zaluzec, X. Zuo, O. J. Borkiewicz, J. M. Hoffman, G. Kwon, A. B. F. Martinson, L. M. Utschig and D. M. Tiede, *ACS Nano*, 2025, **19**, 4170–4185.
20 L. M. Utschig, N. M. Dimitrijevic, O. G. Poluektov, S. D. Chemerisov, K. L. Mulfort and D. M. Tiede, *J. Phys. Chem. Lett.*, 2011, **2**, 236–241.
21 C. J. Gisriel, T. Malavath, T. Qiu, J. P. Menzel, V. S. Batista, G. W. Brudvig and L. M. Utschig, *Nat. Commun.*, 2024, **15**, 9519.
22 M. Gorka, J. Schartner, A. Van Der Est, M. Rögner and J. H. Golbeck, *Biochemistry*, 2014, **53**, 2295–2306.
23 T. D. Rumbaugh, M. J. Gorka, C. S. Baker, J. H. Golbeck and A. Silakov, *Proc. Natl. Acad. Sci. U. S. A.*, 2024, **121**, e2400267121.
24 Z. Xu, S. Wang, C. Zhao, S. Li, X. Liu, L. Wang, M. Li, X. Huang and S. Mann, *Nat. Commun.*, 2020, **11**, 5985.
25 Z. Xu, J. Qi, S. Wang, X. Liu, M. Li, S. Mann and X. Huang, *Nat. Commun.*, 2023, **14**, 1872.
26 T. Noji, M. Kondo, T. Jin, T. Yazawa, H. Osuka, Y. Higuchi, M. Nango, S. Itoh and T. Dewa, *J. Phys. Chem. Lett.*, 2014, **5**, 2402–2407.
27 T. Noji, T. Jin, M. Nango, N. Kamiya and Y. Amao, *ACS Appl. Mater. Interfaces*, 2017, **9**, 3260–3265.
28 T. Noji, T. Suzuki, M. Kondo, T. Jin, K. Kawakami, T. Mizuno, H. Oh-oka, M. Ikeuchi, M. Nango, Y. Amao, N. Kamiya and T. Dewa, *Res. Chem. Intermed.*, 2016, **42**, 7731–7742.
29 T. Noji, K. Kawakami, J.-R. Shen, T. Dewa, M. Nango, N. Kamiya, S. Itoh and T. Jin, *Langmuir*, 2016, **32**, 7796–7805.
30 A. Goyal, S. Szewczyk, G. Burdziński, M. Abram, J. Kargul and K. Gibasiewicz, *Photochem. Photobiol. Sci.*, 2022, **21**, 319–336.
31 A. A. Petrova, G. E. Milanovsky, I. A. Volkhin, M. A. Kozuleva, D. A. Cherepanov and A. Y. Semenov, *Photosynth. Res.*, 2025, **164**, 1.
32 C. Kamidaki, T. Kondo, T. Noji, T. Itoh, A. Yamaguchi and S. Itoh, *J. Phys. Chem. B*, 2013, **117**, 9785–9792.

33 F. Müh and A. Zouni, *Biochim. Biophys. Acta, Bioenerg.*, 2005, **1708**, 219–228.
34 T. Yazawa, H. Tanaka, K. Eguchi and S. Yokoyama, *J. Mater. Sci.*, 1994, **29**, 3433–3440.
35 H. Tanaka, T. Yazawa, K. Eguchi, H. Nagasawa, N. Matsuda and T. Einishi, *J. Non-Cryst. Solids*, 1984, **65**, 301–309.
36 S. Chen and K. Kimura, *J. Phys. Chem. B*, 2001, **105**, 5397–5403.
37 B. Miroux and J. E. Walker, *J. Mol. Biol.*, 1996, **260**, 289–298.
38 A. Diaz, F. Navarro, M. Hervas, J. A. Navarro, S. Chavez, F. J. Florencio and M. A. De la Rosa, *FEBS Lett.*, 1994, **347**, 173–177.
39 E. Arslan, H. Schulz, R. Zufferey, P. Künzler and L. Thöny-Meyer, *Biochem. Biophys. Res. Commun.*, 1998, **251**, 744–747.
40 J. Gómez-Blanco, J. M. de la Rosa-Trevín, R. Marabini, L. Del Cano, A. Jiménez, M. Martínez, R. Melero, T. Majtner, D. Maluenda, J. Mota, Y. Rancel, E. Ramírez-Aportela, J. L. Vilas, M. Carroni, S. Fleischmann, E. Lindahl, A. W. Ashton, M. Basham, D. K. Clare, K. Savage, C. A. Siebert, G. G. Sharov, C. O. S. Sorzano, P. Conesa and J. M. Carazo, *J. Struct. Biol.*, 2018, **204**, 457–463.
41 C. O. S. Sorzano, R. Marabini, J. Velázquez-Muriel, J. R. Bilbao-Castro, S. H. W. Scheres, J. M. Carazo and A. Pascual-Montano, *J. Struct. Biol.*, 2004, **148**, 194–204.
42 R. Fernandez-Leiro and S. H. W. Scheres, *Acta Crystallogr., Sect. D: Struct. Biol.*, 2017, **73**, 496–502.
43 B. V. Trubitsin, M. D. Mamedov, A. Y. Semenov and A. N. Tikhonov, *Photosynth. Res.*, 2014, **122**, 215–231.
44 L. O. Pålsson, C. Flemming, B. Gobets, R. van Grondelle, J. P. Dekker and E. Schlodder, *Biophys. J.*, 1998, **74**, 2611–2622.
45 G. A. Truesdale and A. L. Downing, *Nature*, 1954, **173**, 1236.